

Magnetic skyrmion artificial synapse for neuromorphic computing

Authors: Kyung Mee Song,¹ Jae-Seung Jeong,² Sun Kyung Cha,¹ Tae-Eon Park,¹ Kwangsu Kim,^{1,3} Simone Finizio,⁴ Joerg Raabe,⁴ Joonyeon Chang,¹ Hyunsu Ju,² Seonghoon Woo^{5*}

Affiliations.

¹Center for Spintronics, Korea Institute of Science and Technology, Seoul 02792, Korea

²Center for Opto-Electronic Materials and Devices, Korea Institute of Science and Technology, Seoul 02792, Korea

³Department of Physics, University of Ulsan, Ulsan 44610, Korea

⁴Swiss Light Source, Paul Scherrer Institut, 5232 Villigen, Switzerland

⁵IBM T.J. Watson Research Center, 1101 Kitchawan Rd, Yorktown Heights, New York 10598, USA

*correspondence to: shwoo@ibm.com

Abstract.

Since the discovery of magnetic skyrmions achieved one decade ago, there have been significant efforts to bring the virtual particles into fully functional devices, inspired by their fascinating physical and topological properties suitable for future low-power electronics. Here, we experimentally demonstrate one of such devices – skyrmion-based artificial synaptic device designed for neuromorphic computing. We present that controlled current-induced creation, motion, detection and deletion of skyrmions in ferrimagnetic multilayers can be harnessed to imitate the behaviors of biological synapses. Moreover, we demonstrate that such skyrmion-based synapses can be used to perform neuromorphic pattern-recognition computing using handwritten recognition data set, reaching to the accuracy of ~89%, comparable to the software-based training accuracy of ~93%. Our findings experimentally illustrate the basic concepts of skyrmion-based electronic devices while opening the door to topological magnetic texture-based neuromorphic computing.

Magnetic skyrmions are topologically nontrivial swirling spin textures that exhibit fascinating physical characteristics and have considerable potential as the basis for highly energy-efficient data storage, processing and transmission devices¹. Skyrmions were first observed at ultralow temperatures in magnetic compounds such as MnSi^{2,3} and FeCoSi⁴, whose non-centrosymmetric B20 crystal structure gives rise to an anti-symmetric exchange interaction between neighboring spins, called Dzyaloshinskii-Moriya interaction (DMI)^{5,6}. It has also been found that skyrmions can exist at room temperature in sputtered thin films and multilayers such as Ta/CoFeB/TaOx⁷, Pt/CoFeB/MgO⁸, Ir/Co/Pt⁹ and Pt/Co/MgO¹⁰, stabilized by interface-oriented DMI, perpendicular magnetic anisotropy (PMA), and stray fields. More recently, their electrical creation¹¹⁻¹⁴, motion^{7,8,11,15}, detection^{16,17} and deletion¹⁴ have been separately demonstrated in various material platforms, suggesting that it might be possible to create a fully functional skyrmion-based electronic device that has remained elusive so far. Here, we present such electronic device for the first time, where skyrmions are written, driven, read and erased electrically on a single device at room temperature.

In particular, we demonstrate a skyrmion-based artificial synaptic device designed for neuromorphic computing and thus artificial neural network (ANN), which could be used in broader technology fields in the future. Neuromorphic computing, inspired by the human brain's biological nervous system, has recently attracted significant attention across diverse scientific and technology areas. Extremely low-power consumption is achievable in such system due to the massively paralleled nature operated by neurons (computing elements) and synapses (memory elements)¹⁸. Since the analog memory capability is required for synaptic operations, several existing non-volatile memory (NVM) technology have attempted to emulate the biological synapse including phase-change¹⁹ and resistive²⁰ devices. Spintronics-based synaptic devices have also been

suggested using magnetic domain walls²¹, where the displacement of domain walls could generate multi-resistance states across magnetic tunnel junctions (MTJs). However, the relatively large threshold current for domain wall motion and their stochastic pinning/depinning nature may limit the device performances. Unlikely, skyrmions show rigid-body and particle-like behaviors²², so that multiple nanoscale skyrmions can accumulate within a defined device area without interacting with topographic defects, exhibiting potential for analog storage devices as recently simulated in Ref. [23]. In this work, we experimentally demonstrate that skyrmions can be used for neuromorphic computing by realizing such skyrmion-based artificial synapse.

[Pt (3 nm)/Gd₂₄Fe_{66.6}Co_{9.4} (9 nm)/MgO (1 nm)]₂₀ ferrimagnetic multilayer stacks (Pt/GdFeCo/MgO hereafter) with PMA were studied with high-resolution scanning transmission X-ray microscopy (STXM) [see 24 for material and measurement details]. This asymmetric ferrimagnetic multilayer stack is known to have reasonably large DMI, $|D| = 0.98 \text{ mJ/m}^2$, where $\sim 200 \text{ nm}$ -size skyrmions can be stabilized at room temperature¹⁵. Moreover, electrical writing/deleting from natural sites¹⁴ and efficient skyrmion motion with a reduced skyrmion Hall effect¹⁵ have been individually observed in this ferrimagnetic stack in our previous studies, which are combined together to realize fully functional skyrmion devices in the present work.

Figure 1A shows the experimental set-up used for the simultaneous resistance measurement and domain imaging. Two circuits for electrical pulse application and the device resistance measurement were alternately used. Magnetic domain images of the device were also recorded after each pulse application by probing the transmitted X-ray intensity at the Fe L_3 absorption edge, where X-ray magnetic circular dichroism (XMCD) provides contrasts corresponds to the out-of-plane projection of the magnetization. A scanning electron microscopy (SEM) micrograph of the measured device is included in Fig. 1A, where the blue-colored circular

area denotes the effective synaptic device region where the resistance variations upon magnetization reversal are measured in this Hall-cross geometry [see 24 for the details on active device area calculation].

Figure 1B and 1C show the measured Hall resistances and magnetic domain configurations as a function of out-of-plane magnetic field, B_z , respectively. The same analysis method used in [Ref. 17] was employed for the investigation of the skyrmion-induced change in the Hall resistivity. In Fig. 1B, R_{xy} refers to the measured Hall resistance and $R_{xy,sat}$ refers to the Hall resistance at the saturated state, which corresponds to a Hall bar with a completely black XMCD contrast at $B_z = 160$ mT. Figure 1B also plots the normalized out-of-plane magnetization of Fe atoms, $M_{z,Fe}/M_{z,Fe,sat}$, computed from the domain area of STXM images at each magnetic field (Fig. 1C) [see 17,24 for details]. It should be noted that the magnetic moment of Fe (Gd) aligns (anti-)parallel with the external magnetic field at room temperature, which is higher than the measured magnetization compensation point of this material, $T_M \approx 190$ K [see 24 for details]. Both normalized Hall resistance ($R_{xy}/R_{xy,sat}$) and out-of-plane magnetization ($M_{z,Fe}/M_{z,Fe,sat}$) exhibit a linear dependence with respect to the applied magnetic field, indicating that the measured resistances are reflected by the changes in the out-of-plane magnetic configuration.

While the Hall resistivity of such magnetic material is given by the sum of the ordinary (ρ_{xy}^N), the anomalous (ρ_{xy}^A) and the topological (ρ_{xy}^T) Hall resistivities^{16,17,22}, the magnitude of topological Hall effect (THE) could be suppressed in ferrimagnetic multilayers because the THE contributions two sublattices are destructive due to their antiferromagnetically coupling²⁵. Even considering the presence of a THE contribution, as magneto-transport properties may be dominated by the participating electrons of FeCo because the $4f$ shell of Gd locates below the Fermi energy level, this will still be giving a contribution to the total Hall resistivity which will

depend on the number of skyrmions present in the active area of the sample. This provides a flexibility to our design, allowing its use independently on whether the skyrmions are stabilized in a ferri- or ferromagnetic material. We experimentally measured the ordinary Hall resistance contribution and confirmed its negligible contribution [see 24 for details]. With these established electrical measurement and X-ray magnetic imaging technique, we next examine the behaviors of this artificial synapse.

Figure 2A illustrates the schematic of a skyrmion-based artificial synapse and its working principle, where skyrmions play the role of neurotransmitters in biological systems. In a skyrmion synapse, the synaptic weights are proportional to the number of skyrmions in synapse. Therefore, the electric current-controlled accumulation and dissipation of skyrmions within an active synaptic device area can imitate the linear variations of synaptic weights during potentiation and depression, respectively. Figure 2B demonstrates the experimentally measured electrical operation of a skyrmion synapse, where the corresponding magnetic configuration of each resistance state is also imaged by STXM as shown in Fig. 2C. After applying the initial saturating magnetic field of $B_z = 160$ mT, the field was reduced to $B_z = 140$ mT (image #1 in Fig. 2C). Although this magnetic field still provides enough energy to keep the saturated magnetization, the reduced field opens a room for metastable state, where skyrmions could remain stable once they are generated due to the annihilation energy barrier²⁶.

During potentiation, each image shown in Fig. 2C was acquired after injecting current pulses with the gradually increasing current-density amplitudes of $1.69 \times 10^{10} \text{ A m}^{-2} < |j_a| < 4.24 \times 10^{10} \text{ A m}^{-2}$ and pulse duration of 100 ns, with the polarity as indicated in Fig. 2B inset. The applied unipolar pulses during both potentiation and depression were designed and optimized to generate/delete the controlled number of skyrmions using current-induced spin-orbit torques

(SOTs) as investigated in our previous study¹⁴, assisted by current-induced joule heating that contributes to the reduction of skyrmion switching thresholds²⁷. In Fig. 2B, it is first noticeable that the continuous pulse application systematically generates skyrmions and drives them into the active synapse area, leading to the accumulation of skyrmions and corresponding linear resistance decrease. The first few skyrmions are generated from local pinning sites where nucleation barrier is relatively low, while the majority of skyrmions are generated near the electrical contacts and move across Hall cross area as can be seen in Fig. 2C images #1-#8. Our experiment demonstrates a total of 24 different resistivity states during potentiation. It should be noted that the skyrmion propagation direction is along the current flow direction (against electron flow), and the observed directionality agrees with the behaviors of Néel-type skyrmions with left-handed chirality^{8,15}, proving the topological nature of this material. We have calculated the average resistivity decrease induced by each skyrmion addition over all acquired states during potentiation, $|\Delta\rho_{xy,sk-p}| = \sum_{i=1}^{25} \frac{\Delta\rho_{xy,i}}{N_{sk,i}} / \sum_{i=1}^{25} i = 8.1 \pm 1.7 \text{ n}\Omega \text{ cm}$, where i and N_{sk} denote the state number and the number of skyrmions at each state, respectively. The accumulation of a total of 41 skyrmions [see 24 for details on skyrmion number calculation] leads to the final state $\Delta\rho_{xy,f} = -3.1 \times 10^2 \pm 4.1 \text{ n}\Omega \text{ cm}$ (note that the initial state corresponds to $\Delta\rho_{xy,i} = 0 \text{ n}\Omega \text{ cm}$).

During depression, we simply reversed the polarity of gradually increasing pulses with the same amplitudes and durations (as indicated in Fig. 2B) at a slightly increased background magnetic field $B_z = 144 \text{ mT}$, so that reversed pulses could excite skyrmion texture, eventually leading to skyrmion annihilation mediated by topological defects without creating additional skyrmions¹⁴. Note that strong inter-skyrmion repulsive forces at highly skyrmion-populated states may also contribute to the annihilation upon SOT application, as local impurities in real materials may block their synchronous motion. We indeed observe that the application of serial reversed

pulses systematically annihilates skyrmions (images #9-#16) and leads to the linear resistance increase (Fig. 2B), generating 16 different states with an average resistivity change per skyrmion of $|\Delta\rho_{xy,sk-d}| = 8.9 \pm 0.1 \text{ n}\Omega \text{ cm}$ during depression, in agreement with $|\Delta\rho_{xy,sk-p}|$ measured for potentiation.

The number of skyrmions at each resistivity state is also plotted together in Fig. 2B. It is noteworthy that the measured resistivity change is slightly deviated from the corresponding skyrmion number variation especially at highly populated states, and as noted above, we believe this deviation is caused by the statistical distribution in skyrmion diameter affected by local defects and their mutual interactions. For example, at largely accumulated states (near image #8 in Fig. 2C), stronger mutual repulsive interactions between skyrmions lead to the reduction in the average skyrmion diameter, $d_{sk} = 256 \pm 25 \text{ nm}$, compared to their initial distribution at sparse distribution (image #5 in Fig. 2C), $d_{sk} = 285 \pm 25 \text{ nm}$ [see 24 for the details of skyrmion diameter calculation]. Considering that the skyrmion diameter is a fixed value at a defined magnetic field in a defect-free material reflecting the equilibrium at given energetic contributions²⁶, further material optimization could overcome the limitation and thus present complete linearity depending on the number of skyrmions. Nevertheless, the observed linear resistance variation clearly presents the key behavior of skyrmion-based artificial synapse: the current-induced analog synaptic weight modulation. We also demonstrate ‘set’ and ‘reset’ operations that are required for the programmable flexibility of an artificial synapse [see 24 for details].

With these measured characteristics of skyrmion-based artificial synapse, we simulated an ANN to perform the pattern recognition, where a multilayer perceptron algorithm is used to learn the Modified National Institute of Standards and Technology (MNIST) handwritten pattern data set²⁸. Figure 3 presents a simulation platform and the result of pattern recognition accuracy. Figure

3A first depicts the neural network used for learning the MNIST data consisting of 3 layers: input neural layer of 784 neurons, hidden layer of 100 neurons and output layer of 10 neurons, and skyrmion synapses are used during trainings as schematically described in Fig. 3B [see 24 for neural network simulation details]. Figure 3C shows the simulated pattern recognition accuracy as a function of training iteration for skyrmion synapse-based ANN, and the result for software-based ANN is also plotted for comparison. Our simulation demonstrates that the ANN composed of skyrmion synapses can reach ~89% pattern recognition accuracy, which is comparable to the accuracy of ideal software-based training, ~93% (Fig. 3C). Figure 3D presents the resistivity distributions translated from the synaptic weights before and after training operations. It is noteworthy that the non-ideal characteristics of demonstrated skyrmion synapses, e.g. small on/off ratio, limited number of resistance levels and cycle-to-cycle variations, may have limited the accuracy of ANN and caused stochastic behavior observed in Fig. 3C. However, the overall device performance of skyrmion synapses could further be optimized and enhanced, by adopting recent findings such as ~10 nm-size skyrmion at compensated ferrimagnets²⁹ or new electrical skyrmion-reading scheme using magnetic tunnel junctions (MTJs)³⁰, which together would dramatically increase the scalability and electrical characteristics of skyrmion synapses.

Our results demonstrate a fully functional skyrmion-based electronic device – skyrmion-based artificial synapse – by incorporating current-induced skyrmion creation, motion, detection and deletion techniques in a single ferrimagnetic device scheme. Moreover, we present that the skyrmion synapse, where synaptic weights are modulated by the number of skyrmions in an active device area, can be implemented for the neuromorphic computing simulation of supervised pattern recognition, reaching a high learning accuracy of ~89%. This work paves the new avenue towards

skyrmion-based electronics while highlighting the possibility to use topological magnetic textures for neuromorphic computing devices.

References and Notes:

1. Fert, A., Reyren, N. & Cros, V. Magnetic skyrmions: advances in physics and potential applications. *Nat. Rev. Mater.* **2**, 17031 (2017).
2. Mühlbauer, S. *et al.* Skyrmion Lattice in a Chiral Magnet. *Science* **323**, 915–919 (2009).
3. Schulz, T. *et al.* Emergent electrodynamics of skyrmions in a chiral magnet. *Nat. Phys.* **8**, 301–304 (2012).
4. Yu, X. Z. *et al.* Real-space observation of a two-dimensional skyrmion crystal. *Nature* **465**, 901–904 (2010).
5. Dzyaloshinsky, I. A thermodynamic theory of “weak” ferromagnetism of antiferromagnetics. *J. Phys. Chem. Solids* **4**, 241–255 (1958).
6. Moriya, T. Anisotropic Superexchange Interaction and Weak Ferromagnetism. *Phys. Rev.* **120**, 91–98 (1960).
7. Jiang, W. *et al.* Blowing magnetic skyrmion bubbles. *Science* **349**, 283–286 (2015).
8. Woo, S. *et al.* Observation of room-temperature magnetic skyrmions and their current-driven dynamics in ultrathin metallic ferromagnets. *Nat. Mater.* **15**, 501–506 (2016).
9. Moreau-Luchaire, C. *et al.* Additive interfacial chiral interaction in multilayers for stabilization of small individual skyrmions at room temperature. *Nat. Nanotechnol.* **11**, 444–448 (2016).
10. Boulle, O. *et al.* Room-temperature chiral magnetic skyrmions in ultrathin magnetic nanostructures. *Nat. Nanotechnol.* **11**, 449–454 (2016).
11. Legrand, W. *et al.* Room-Temperature Current-Induced Generation and Motion of sub-100 nm Skyrmions. *Nano Lett.* **17**, 2703–2712 (2017).

12. Hrabec, A. *et al.* Current-induced skyrmion generation and dynamics in symmetric bilayers. *Nat. Commun.* **8**, 15765 (2017).
13. Büttner, F. *et al.* Field-free deterministic ultrafast creation of magnetic skyrmions by spin-orbit torques. *Nat. Nanotechnol.* **12**, 1040–1044 (2017).
14. Woo, S. *et al.* Deterministic creation and deletion of a single magnetic skyrmion observed by direct time-resolved X-ray microscopy. *Nat. Electron.* **1**, 288 (2018).
15. Woo, S. *et al.* Current-driven dynamics and inhibition of the skyrmion Hall effect of ferrimagnetic skyrmions in GdFeCo films. *Nat. Commun.* **9**, 959 (2018).
16. Maccariello, D. *et al.* Electrical detection of single magnetic skyrmions in metallic multilayers at room temperature. *Nat. Nanotechnol.* **13**, 233 (2018).
17. Zeissler, K. *et al.* Discrete Hall resistivity contribution from Néel skyrmions in multilayer nanodiscs. *Nat. Nanotechnol.* **13**, 1161 (2018).
18. Hopfield, J. J. Neural networks and physical systems with emergent collective computational abilities. *Proc. Natl. Acad. Sci.* **79**, 2554–2558 (1982).
19. Kuzum, D., Jeyasingh, R. G. D., Lee, B. & Wong, H.-S. P. Nanoelectronic Programmable Synapses Based on Phase Change Materials for Brain-Inspired Computing. *Nano Lett.* **12**, 2179–2186 (2012).
20. Prezioso, M. *et al.* Training and operation of an integrated neuromorphic network based on metal-oxide memristors. *Nature* **521**, 61–64 (2015).
21. Lequeux, S. *et al.* A magnetic synapse: multilevel spin-torque memristor with perpendicular anisotropy. *Sci. Rep.* **6**, 31510 (2016).
22. Nagaosa, N. & Tokura, Y. Topological properties and dynamics of magnetic skyrmions. *Nat. Nanotechnol.* **8**, 899–911 (2013).

23. Huang, Y., Kang, W., Zhang, X., Zhou, Y. & Zhao, W. Magnetic skyrmion-based synaptic devices. *Nanotechnology* **28**, 08LT02 (2017).
24. Supplementary materials are available in online version of this article.
25. Barker, J. & Tretiakov, O. A. Static and Dynamical Properties of Antiferromagnetic Skyrmions in the Presence of Applied Current and Temperature. *Phys. Rev. Lett.* **116**, 147203 (2016).
26. Büttner, F., Lemesh, I. & Beach, G. S. D. Theory of isolated magnetic skyrmions: From fundamentals to room temperature applications. *Sci. Rep.* **8**, 4464 (2018).
27. Finizio, S. *et al.* Deterministic field-free skyrmion nucleation at a nano-engineered injector device. *ArXiv190210435 Cond-Mat* (2019).
28. Chen, P.-Y., Peng, X. & Yu, S. NeuroSim+: An integrated device-to-algorithm framework for benchmarking synaptic devices and array architectures - IEEE Conference Publication. *2017 IEEE Int Electron Devices Meet. IEDM* 6.1.1–4 (2017).
doi:10.1109/IEDM.2017.8268337
29. Caretta, L. *et al.* Fast current-driven domain walls and small skyrmions in a compensated ferrimagnet. *Nat. Nanotechnol.* **13**, 1154 (2018).
30. Tomasello, R. *et al.* Electrical detection of single magnetic skyrmion at room temperature. *AIP Adv.* **7**, 056022 (2017).

Acknowledgments.

This work was mainly supported by KIST Institutional Program and IBM Research. S.W. acknowledges management support from Guohan Hu and Daniel Worledge. S.W. also acknowledges Xichao Zhang, Sanghoon Kim, Yan Zhou and Motohiko Ezawa for reading manuscript and providing important thoughts and Ki-Young Lee for providing artworks included in Figure 2. K.M.S., S.K.C., T.-E.P. and J.C. acknowledge the support from the National Research Council of Science and Technology (NST) (Grant no. CAP-16-01-KIST) by the Korean government (MSIP). K.K. acknowledges the support from the Basic Research Laboratory Program through the National Research Foundation of Korea (NRF) funded by the MSIT(NRF-2018R1A4A1020696). J.-S.J. and H.J. acknowledge the support from the Korea National Research Foundation program (NRF-2017R1E1A1A01077484), particularly utilized to conduct the MNIST pattern learning works of this research. The PolLux endstation was financed by the German Bundesministerium für Bildung und Forschung under grant No. 05KS7WE1.

Author contributions. S.W. designed, planned and initiated the study. K.M.S. grew films, fabricated devices and performed initial device characterizations. S.K.C. provided device fabrication support using electron beam lithography. S.W., K.M.S., T.-E.P, K.S.K., S.F. and J.R. performed STXM experiments at Swiss Light Source in Villigen, Switzerland. J.-S.J. and H.J. performed the neuromorphic computing simulation work. K.M.S., H.J. and S.W. drafted the manuscript and all authors reviewed the manuscript.

Competing Interests: The authors declare no competing interests.

Figures.

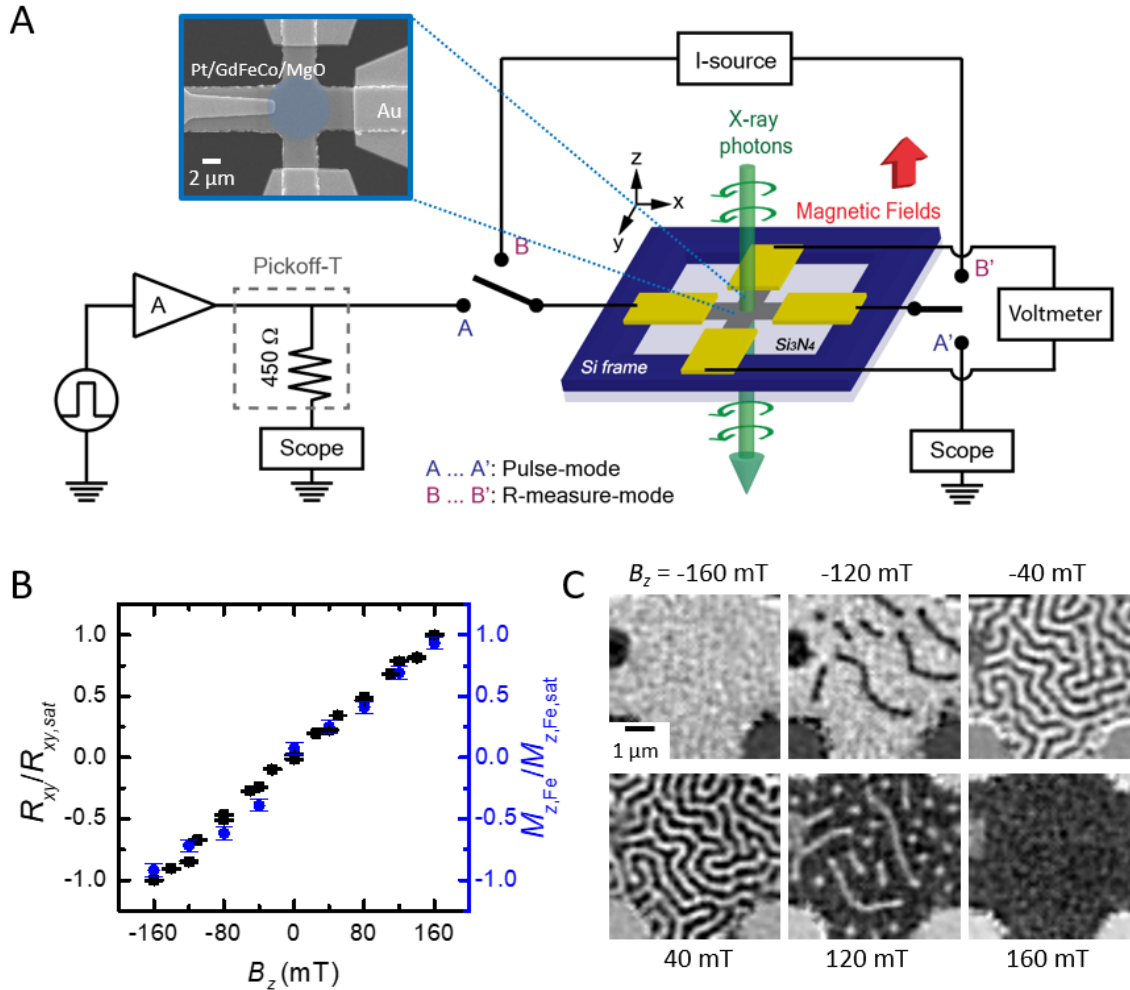


Figure 1. Schematic of the experimental set-up and X-ray imaging of domain structures. (A) Schematic of scanning transmission X-ray microscopy (STXM) and simultaneous electrical measurement geometry. Scanning electron microscope image of the measured device is enclosed, and the marked circular area denotes the effective area where the Hall bar resistance was measured [see ²⁴ for details]. The A-A' connection is used for electrical pulse applications along the horizontal stripe (along x -axis) of the Hall bar geometry, while the B-B' connection is used for subsequent resistance measurements along the vertical (along y -axis) Hall bar contacts. **(B)** The measured Hall resistance ($R_{xy}/R_{xy,sat}$) and the extracted out-of-plane magnetization of Fe atoms ($M_{z,Fe}/M_{z,Fe,sat}$) as a function of applied magnetic field, B_z . Error bars indicate the standard deviation of 10 individual resistivity measurements ($R_{xy}/R_{xy,sat}$) and spatial resolution and counting statistics ($M_{z,Fe}/M_{z,Fe,sat}$). **(C)** Exemplary STXM images acquired at several out-of-plane magnetic fields, B_z . Dark and bright contrast correspond to Fe-magnetization oriented up (along $+z$) and down (along $-z$), respectively. Note that Fe (Gd) moments are aligned (anti-)parallel to magnetic fields as the measurements were conducted above the magnetization compensation temperature, $T_M \approx 190$ K, of this material as discussed in 24.

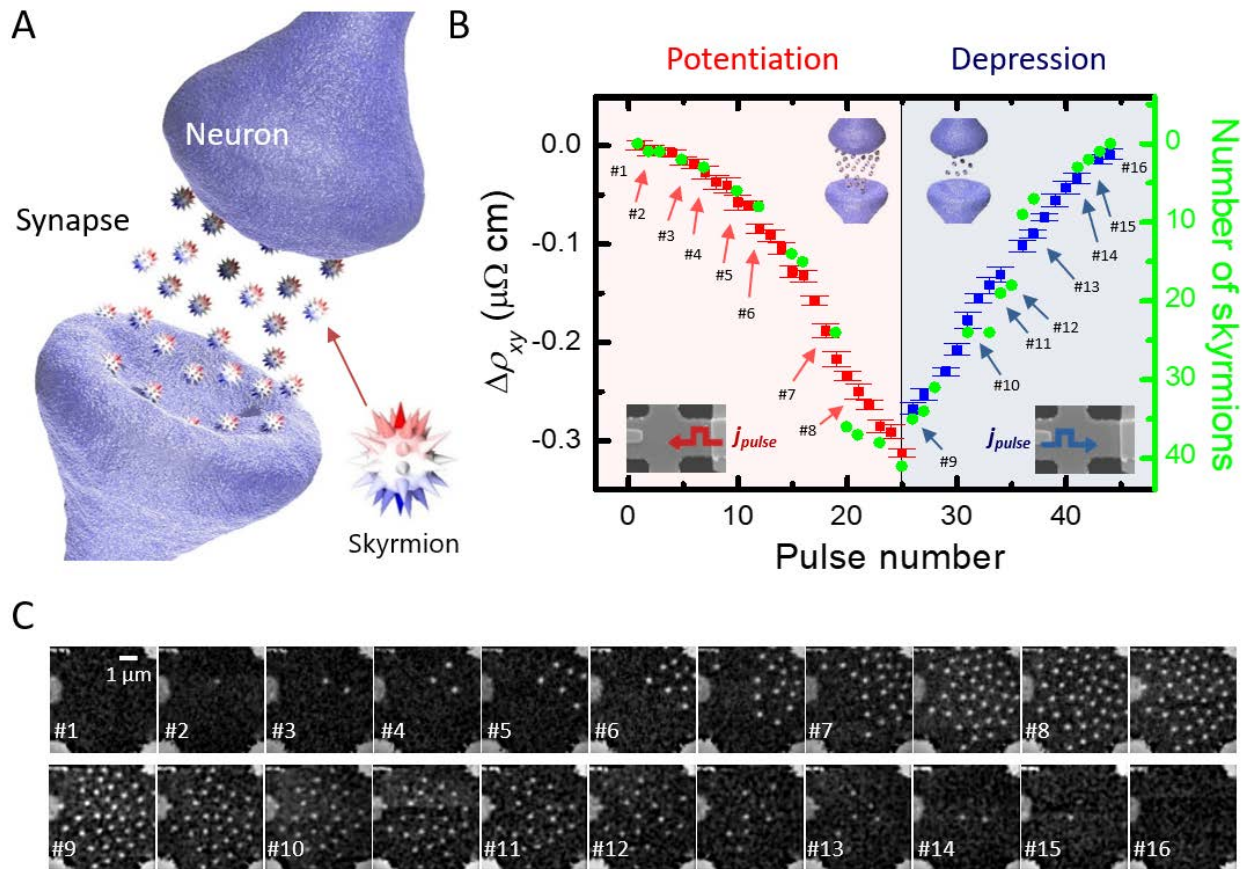


Figure 2. Magnetic skyrmion-based artificial synapse. (A) Schematic drawing of skyrmion-based artificial synapse and its working principle. The red and blue colored arrows represent magnetic moments pointing $+z$ and $-z$ directions within skyrmions, respectively. (B) The measured Hall resistivity change and calculated skyrmion number as a function of injected pulse number. Note that red and blue symbols and colored areas correspond to resistivity changes (left axis) during potentiation and depression, respectively. Green symbols are used to indicate the number of skyrmions corresponding to right axis. Enclosed electrical pulses indicate the direction of charge current pulse, opposite to the direction of electron flow. Error bars denote the standard deviation of the resistivity measurements at each state. (C) Sequential STXM images showing skyrmion populations after injecting unipolar current pulses along the track, with polarities as indicated in (B). Upper and lower panels show domain images during potentiation and depression, respectively, and each image number, #1-#16, corresponds to each resistivity state indicated in (B).

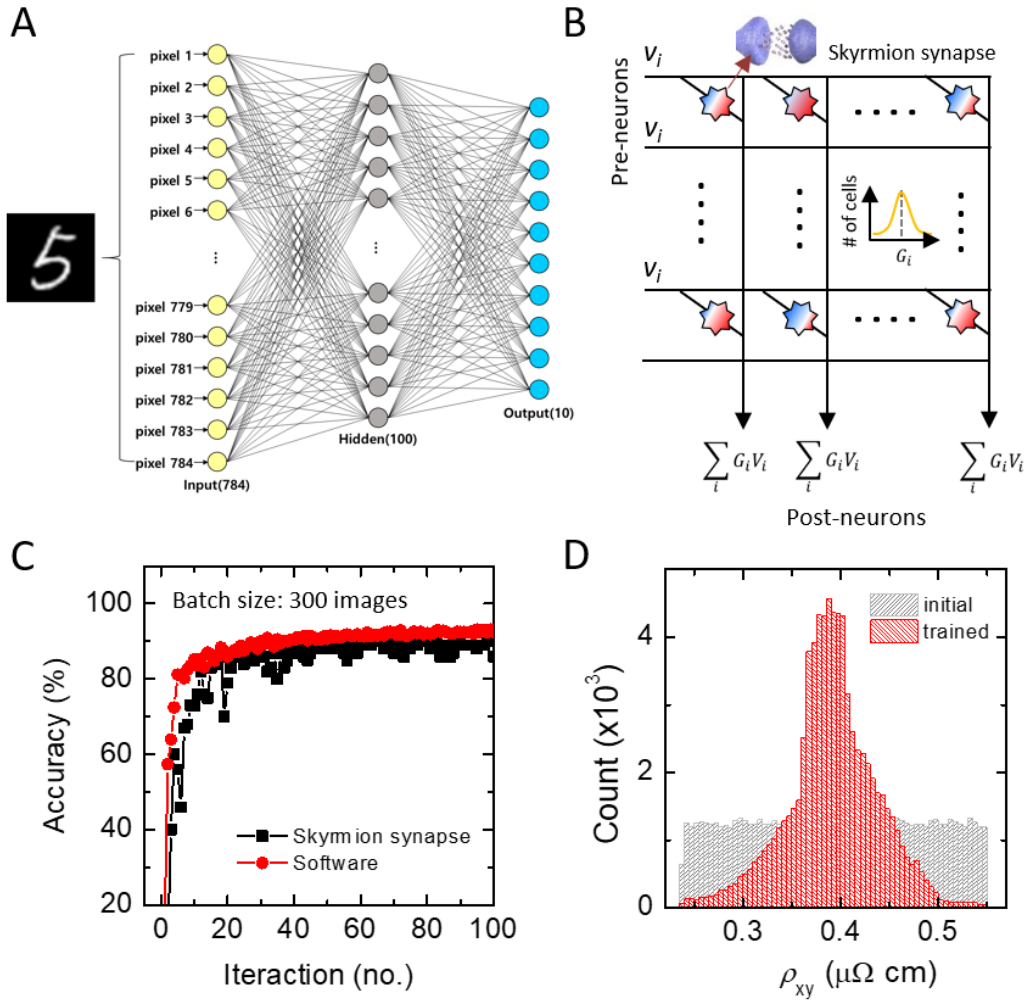


Figure 3. The pattern recognition simulation using skyrmion synapse. (A) The structure of tri-layer neural networks consists of 784 input neurons, 100 hidden neurons and 10 output neurons. (B) Schematic of circuit diagram comprising skyrmion-based synapses. At each conductance level, the conductance values of skyrmion synapses follow the normal distribution with the average and the deviation, G_i and σ_i , whenever synaptic weights update. (C) Evolution of pattern recognition accuracy as a function of training iteration for an idea (software-based) and a skyrmion-based synaptic device, where the batch size of 300 images is used for each iterative training. (D) Distribution of skyrmion synapse resistivity before- and after- trainings.